Controlling Pollutant Emissions in a High-Pressure Combustor with Fuel-Diluent Blending

Bernhard Stiehl
University of Central Florida
4000 Central Florida Blvd, Orlando, FL 32816
bernhard.stiehl@ucf.edu

Anthony Morales
University of Central Florida
4000 Central Florida Blvd, Orlando, FL 32816
anthony.morales@ucf.edu

Tommy Genova
University of Central Florida
4000 Central Florida Blvd, Orlando, FL 32816
tommy.genova@ucf.edu

Michelle Otero
University of Central Florida
4000 Central Florida Blvd, Orlando, FL 32816
motero0508@gmail.com

Scott Martin
Embry-Riddle Aeronautical University
600 S Clyde Morris Blvd, Daytona Beach, FL 32114
martis38@erau.edu

Changjin Yoon
GE Global Research
1 Research Cir, Niskayuna, NY 12309
changjin.yoon@ge.com

Kareem Ahmed
University of Central Florida
4000 Central Florida Blvd, Orlando, FL 32816
kareem.ahmed@ucf.edu

ABSTRACT

This paper investigates the formation of nitric oxide (NO) and carbon monoxide (CO) emissions as a function of nitrogen (N_2) or carbon dioxide (CO_2) diluent content, added to a premixed reacting jet in crossflow. Reaction characteristics of a rich methane-air-diluent jet injected into a lean vitiated crossflow were analyzed at an elevated pressure level 5 atm, which is critical to obtain data scalable to industry conditions. The jet was pre-heated and enriched with 0%, 15%, 30%, and 50% dilution by mass percentage to quantify the effect on pollutant emissions. Simulated results of the full chemistry Star-CCM+ CFD model were verified with data taken in an experimental high-pressure combustion facility, which provides pressure, temperature, and velocity profiles, as well as line-of-sight chemiluminescence and exit emission measurements. The analysis revealed the significant influence of the diluent to increase the axial flame lift-off and delay axial combustion. Increasing the diluent content increased the timescale for the flame to stabilize, which allowed for greater entrainment of crossflow oxidizer into the axial jet stream, and led to decreased pollutant emissions. Hence, crossflow entrainment is a critical driving force at high diluent content. Local nitric oxide (NO) emission formation in the axial stage was predicted numerically, showing a correlation between diluent addition, axial heat release, and the formation of nitric oxide pollution. The high diluent levels delayed axial combustion, while reducing prompt and thermal NO_x by mitigating flame hotspots and minimizing the timescale that the products remain at high temperatures.

Keywords: Axial Staged Combustion, Reacting Jet in Crossflow, CO and NO_x Emission, Gas Turbine Combustor, High Pressure, Diluent Blends, Pollutant Emissions

1. INTRODUCTION

With the definition of near-term, ultra-low emission goals for power generation and aviation turbine applications, the advancement of carbon-free combustion technology, and the continuous efforts of original equipment manufacturers (OEMs) to increase the efficiency of their combustion systems, a challenging field of research has developed and been optimized for decades. A widespread technology to decrease turbine emissions is the concept of axial staging, allowing to burn the majority of fuel at relatively uncritical emission temperatures in a main burner stage, which is followed by a subsequent, high-temperature axial burner stage. A schematic of such an after-burner stage, the jet-in-crossflow stage, is shown with CFD simulation in fig. 1, plotting vorticity iso-contours and introduced methane distribution at three positions downstream of an axial jet.

Thermal NO_x is strongly temperature dependent and could form in the hot gas throughout the axial stage. The particularly high temperature sensitivity of thermal NO_x needs to be emphasized, doubling thermal NO_x for a temperature increase of 100K at flame temperatures beyond 2000K. Significant amount of thermal NO_x typically forms at temperatures above 1700K. Operating points in this study would produce local temperatures of 2000K, resulting in thermal NO_x to be the dominant source of NO_x production. Critical equations for thermal NO_x formation are stated

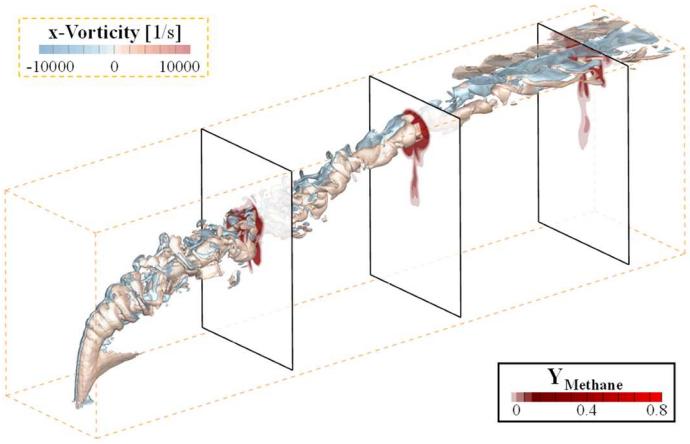

Figure 1: Schematic of jet-in-crossflow numerical modeling with commercial CFD code

in the Zeldovich mechanism [1, 2], shown in eqs. 1-3. Rate constants for these equations could be found in [3, 4]. In contrast, prompt NO_x was initially defined by Fenimore [5] and forms in close proximity ("promptly") by the flame. Prompt NO_x forms in relatively low-temperature, fuel-rich zones at short residence time. According to the most accepted reaction pathway, CH (or CH_2) react with N_2 to form HCN, which reacts further to CN and eventually to NO. A subordinate prompt NO_x route forms NCN, which is not part of the GRI-Mech 3.0 and hence not considered in the present study. Prompt NO_x formation is relatively proportional to the amount of nitrogen radicals present locally. An increased amount of prompt NO_x can be expected with the detailed chemistry simulations in this study due to a relatively large jet diameter, and rich jet equivalence ratio. However, the influence of the diluent as a potential thermal and molecular barrier remains to be investigated and documented in 3D.

$$\mathrm{O} + \mathrm{N_2} \overset{k_{+1}}{\rightleftharpoons} \mathrm{N} + \mathrm{NO} \quad (1)$$

$$\mathrm{N} + \mathrm{O_2} \overset{k_{+2}}{\rightleftharpoons} \mathrm{O} + \mathrm{NO} \quad (2)$$

$$\mathrm{N} + \mathrm{OH} \overset{k_{+3}}{\rightleftharpoons} \mathrm{H} + \mathrm{NO} \quad (3)$$

Technological advancements of axially staged combustion systems were patented by several turbine OEMs, including Siemens [6], GE [7], and MHI. The present paper is targeted to investigate the formation of pollutant emissions specifically for the use of N_2 and CO_2 diluent gases in an axial jet. In a land-based turbine power plant, N_2 diluent could be generated with an air separation unit (ASU), while CO_2 forms as the main product of CH_4 combustion. The exhaust gas could be run through a water separation stage and a $CO_2/N_2/O_2$ mixture at elevated temperature be recirculated to the axial combustion stage with exhaust gas recirculation (EGR).

Studies by [8] investigated the effect of N_2 and Argon diluents on the liftoff of partially premixed, turbulent methane jet flames experimentally. The stability of methane

flames was found to have a high sensitivity to the diluent type due to relatively narrow flammability limits, and lower flame speed relative to other fuels, like ethylene and hydrogen. At increased diluent levels beyond 10%vol, dilution with Argon resulted in a flame that stabilized further downstream relative to N_2-diluted systems. A trend to increase the lift-off distance of the penetrating jet with increasing dilution level was reported [8]. Other experimental studies were performed by [9] and investigated the ignition and flame propagation in CH_4/O_2 flames diluted with CO_2 in a spherical combustion chamber with laser ignition. Laminar burning velocities were obtained over a range of near-stoichiometric equivalence ratios and variable amount of oxygen enrichment. In addition, the effects of air entrainment [10] and diluent addition on the lift-off and blow-off of turbulent jet flames [11] were investigated in the recent literature. The design for a model gas turbine combustor with variable CO_2-doped methane combustion was studied to emulate compositions found in biogas [12], while [13] documented the effect of N_2 and CO_2 diluents on the combustion of syngas. The stabilization of CO_2-diluted, premixed CH_4-O_2 flames was compared to a CH_4-air system experimentally with PIV and OH* chemiluminescence [14]. Similar stabilization characteristics, but a more uniform firing temperature profile distribution were documented for the diluted system. The use of CO_2 diluent added narrower limits to the burner operating regime [14]. The effect of dilution gases CO_2, H_2O, N_2, and full EGR, on the flame structure and laminar flame speed of methane/air systems was investigated numerically by [15], documenting chemical, thermal and dilution effects quantitatively. Further studies on the reduction of laminar flame speeds for premixed CH_4/O_2 systems with N_2 and CO_2 diluents were documented by [16].

The effect of pressure on the increase of laminar burning velocities in lean $H_2/CO/O_2$/diluent systems was studied by [17], while [18] documents the influence of pressure and mixing efficiency of a staged injection system. The dilution of premixed methane-air systems at atmospheric [19] and elevated pressure levels [20] was investigated with pure and mixed flue gases N_2, H_2O and CO_2, proving the high predictive quality of the GRI-Mech 3.0 kinetic mechanism. The validity of GRI-Mech 3.0 [21] was confirmed by validation against ARAMCO Mech 1.3 [22] in Chemkin, and a sensitivity analysis was carried out to determine key reactions that influence the predicted flame speeds [9]. The effect of pressure on the ignition timescales under variable temperature and equivalence ratio was investigated numerically and experimentally with a shock-tube by [23]. A kinetic scheme with 100 reactions was benchmarked for use in detailed chemistry simulations, documenting the reaction rates for CO_2 and N_2 diluents in methane systems [24]. Further methane oxidation schemes with reduced and skeletal kinetic mechanisms were investigated by [25].

Emission studies were performed in a moderate or intense low-oxygen dilution (MILD) combustor for a CH_4 jet flame in hot oxidizer, outlining the nitric oxide emission reduction potential under diluent addition. The increased potential for emission reduction with CO_2 diluent relative to N_2 was attributed to the higher thermal capacity of CO_2, as well as the absence of additional bound nitrogen species [26]. Related studies documented a NO_x reduction potential as a function of equivalence ratio and staging ratio with experimental OH* imaging and emission measurements [27]. Further guidelines on the impact of chemical and radiation effects on the NO_x formation in CO_2-diluted oxy-methane combustion were postulated by [28]. The impact of fuel properties and fuel dilution to

reduce NO_x emission for distributed combustion was studied by [29]. A NO_x emission reduction potential with air staging and reburning in a lab-scale test facility was reported by [30]. Experimental validation data with PIV and OH-PLIF of a staged burner architecture was documented by [31].

A significant amount of research was performed on colorless distributed combustion (CDC), which is a highly-uniform combustion method for biofuels and fossil fuels, with the objective to avoid flame pockets and local zones of high equivalence ratio variation. CDC is achieved by using an oxidizer mixture, tuned specifically to reduce oxygen concentration by addition of high-temperature reactive species. Initial efforts on that field provided recommendations for the fuel-air level of mixedness, as well as for optimal jet momentum flux ratio [32]. CDC studies were developed to include a swirl-assisted, partially premixed burner to combust propane-air mixture that was diluted with N_2 or CO_2 [33]. Further, a study with pre-vaporized liquid fuels in a similar swirl burner architecture tuned for low NO_x emission by [34]. More importantly, studies with methane showed a need for stabilizing heat release fluctuations in swirl assisted oxy-CO_2 methane combustion, which was attained by reducing local oxygen level in the distributed combustion system [35]. The potential to enhance methane flame stability under hydrogen addition, while saving CO emission was documented in [36]. Another follow-up study focused on the oxidizer, determining 25% oxygen and 75% CO_2 as the optimal oxidizer mixture [37]. To precisely track the advancement of CDC technology, state-of the-art experimental diagnostics had to be used for these studies. The effect of air dilution versus modeling lower oxygen entrainment was tracked with PIV [38]. Integral length scales along the flame boundary were determined with OH-PLIF [38]. Secondly,

chemiluminescence was done for CH* and OH* to detect the local equivalence ratio distribution, as well as NO emission was shown to reduce under distributed condition [39]. The details on how the evolution of flame-swirl structure was made visible with OH* chemiluminescence and an advanced image filtering method are provided in [40].

Recent experimental and numerical studies documented the effects of CO_2 on laminar CH_4/air flames for various CO_2 diluent concentration in a co-flow combustor, and analyzed with LIF measurements [41]. A reduced GRI-Mech 3.0 was used in *Ansys Chemkin-Pro* with the 1D opposed flow flame model to validate numerical outcomes against the experimental data. The trend of decreasing CH concentration in the flame and decreasing NO emission production was outlined as the amount of CO_2 diluent was increased [41]. Similarly, an *Ansys Chemkin-Pro* study in reduced dimensionality [6] was conducted to provide the upstream boundary condition for the 3D detailed chemistry model of the present work. The 3D model is targeted to provide spatial insight to the reduction of local reaction rate and pollution levels with increasing diluent content.

2. RESEARCH OBJECTIVE

Motivated by the industrial relevance of the temperature profile generated by axial jets [6], the present paper is targeted to characterize the effect of diluent addition and analyze full chemistry outcomes with respect to the turbine inlet temperature profile and local emission formation. Objective of the present work is the exploration of nitrogen (N_2) or carbon dioxide (CO_2) diluent addition in a premixed axial reacting jet-in-crossflow combustor, emulating high firing temperatures and lean operating condition as seen in modern gas turbines. Studies were performed experimentally in-house for validation and a

Star-CCM+ [42] detailed chemistry computational model is computed in 3D with species transport equations for the full GRI-Mech 3.0 methane-air kinetic mechanism. Insight to the effect of axial diluent addition on the firing temperature profile and outlet pollution levels, as well as the documentation of local nitric oxide formation kinetics could be of high industrial relevance to further optimize existing gas turbine combustor facilities.

3. MATERIALS AND METHODS

The study utilizes a staged combustor architecture, which is described further in section 3.1. The premixed main combustor species composition (blue in fig. 2) is determined with measurements at position (A), and complemented with approximative 0D Equilibrium and 1D Opposite Flow Combustor models in *Ansys Chemkin-Pro*. The second burner stage (axial stage) is modelled with a 3D CFD detailed chemistry model, highlighted in fig. 2 (red color). The staging ratio is about 10:1 by total mass (main burner to axial jet). The study is focused on the second stage emission reduction potential by substituting 15%, 30% and 50% by volume of axial oxidizer air with either N_2 or CO_2 diluent in the premixed axial jet.

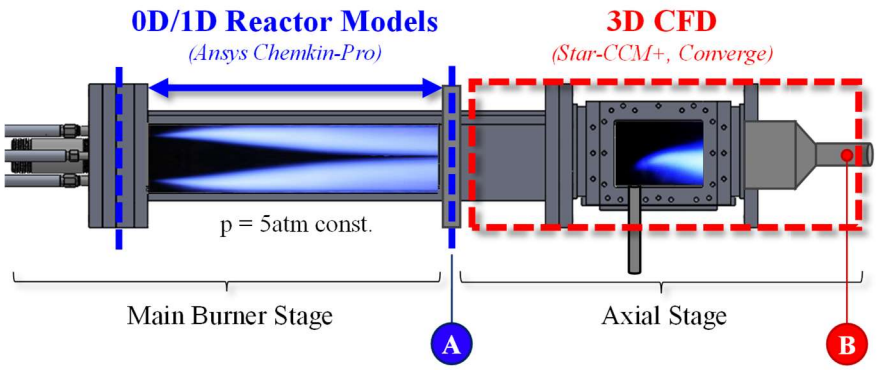

Figure 2: Overview of experimental facility with emission sampling positions (A, B) and modelling strategies indicated for both combustion stages

3.1 Experimental Staged Turbine Combustor Facility

The facility contains a main burner stage, which provides vitiated crossflow to an optically accessible axial stage, highlighted in fig. 3. A detailed description of the experimental facility was provided in previous work [43-45]. Methane and air react under lean conditions in the main burner section, and bypass air is injected coaxially around the main burner pipe to further lean out the vitiated flow. The axial stage consists of an optically accessible test section with two (124*95.2) mm side windows, a (127*40.6) mm bottom window, and a top injector plate with a 12.7 mm diameter wall flush injector. Further minimization of the main burner emission level was achieved using a lower burner equivalence ratio and lower air flows in the main burner bypass. The corrections helped to reduce the main burner NO emission to 6.0ppmvd (corrected to 15% O_2) for the present full-load condition, using a main burner equivalence ratio of 0.75 at a firing temperature level T_{max} = 1800K. To obtain emissions data, an upgraded E-Instruments E4500 gas analyzer was used, capable of measuring NO and NO_2 with a resolution of ±0.8ppmvd for NO and ±4ppmvd for CO, CO_2 and O_2. The measurement positions are indicated with *A* (between burner stages) and *B* (outlet of axial stage) in Fig. 2. To obtain the temperature profile, a c-type thermocouple was introduced with a variable depth compression fitting along the z-symmetry plane at position (A), and data was taken in increments of 1cm. The measurements were repeated three times at each location and deviations remained within 4.5% (cf. Fig. 4). Velocity and turbulence intensity characteristics were recorded with Particle Image Velocimetry (PIV), using a dual-head 532nm Evergreen laser with 3µm aluminum oxide seed particles and an Andor camera to capture 2048*2048px imagery.

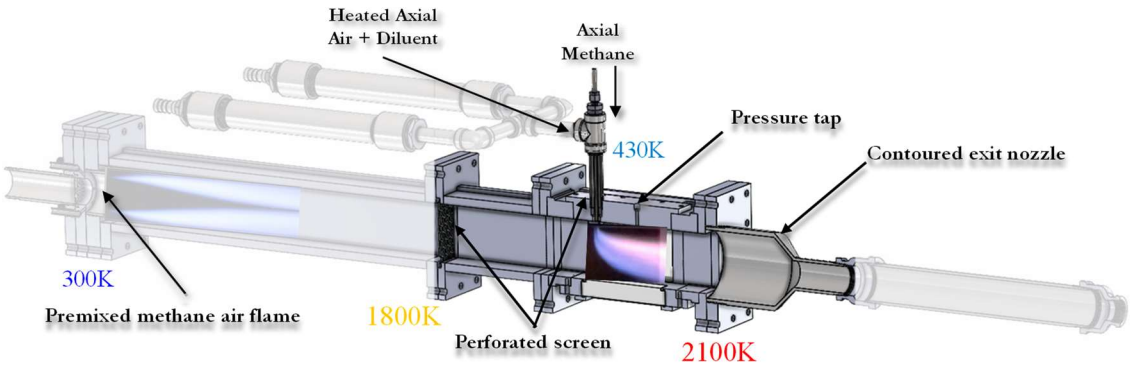

Figure 3: Schematic of experimental axially staged combustion facility with highlighted focus domain for 3D CFD modelling and peak temperature levels indicated

CH* chemiluminescence was taken with a Photron Fastcam SA1.1 at 20,000fps and a 430nm filter [46-48]. Recent facility improvements [49] at the injector include an added flow straightener at the jet inlet to stabilize the penetrating jet hydrodynamically and provide a more defined boundary condition for axial CFD modeling. In order to depict industrially relevant axial jet conditions, two axial heaters were installed to heat the axial air and diluent streams. The CFD model describes the thermal jet boundary condition as a top-hat profile with a pre-heated temperature average of 435K. The flow meters allowed precise adjustment of the diluent content with uncertainty of ±2% (cf. fig. 5).

3.2 Numerical Description

The CFD model focuses on the critical jet-in-crossflow zone, defining the experimental perforated screen positions as mass flow inlets with measured species compositions as well as coupled temperature and velocity profiles.

3.2.1 Computational Models

A previously verified *Star-CCM+* Computational Fluid Dynamics (CFD) model utilizes detailed chemistry with the full GRI-Mech 3.0 methane mechanism, in conjunction

with Reynolds Stress Turbulence (RST) and the Elliptic Blending transition function applied. A comprehensive description of the *Star-CCM+* CFD model used for this paper can be found in [46, 50]. Use of the Laminar Flame Concept was shown to overpredict the local reaction rates at the flame and the local NO_x amount produced [50, 51], hence, the finite-rate detailed chemistry model coupled with the Eddy Dissipation Concept was used. Equation 4 states the right side of the species transport equation, with the species reaction source term ω_i being a function of the chemistry step of species mass fraction Y_i, time step τ, density ρ, and mean reaction rate multiplier f.

$$\omega_i = \rho f \left(\frac{Y_i^* - Y_i}{\tau} \right) \tag{4}$$

Using the Eddy Dissipation Concept, increased turbulence-chemistry interaction is considered by modeling a reaction rate multiplier $f < 1$, defined in eq. 5.

$$f = \left(\left[C_l \left(\frac{\upsilon \tau_{turb}}{L^2} \right)^{0.25} \right]^{-3} - 1 \right)^{-1} \tag{5}$$

The additional turbulence-chemistry interaction term aids resolution of the premixed flame and is implemented with dependencies of kinematic viscosity υ, fine-structure length constant C_l, turbulent length scale L, and turbulent time scale τ_{turb}, reducing the reaction rates relative to the laminar solution [46, 50]. The model choice is in agreement with jet-in-crossflow CFD from the literature [52] and was documented mathematically in previous work [50], allowing the full GRI-Mech 3.0 [21] to be calculated with species transport equations. Turbulent Schmidt and Prandtl numbers were set to 0.5 to account for enhanced turbulent momentum diffusion [53]. Grid convergence was investigated in previous work [46] and shown to be relatively insensitive between Δs_{min} = 0.25mm and 0.5mm cubical cell size in the reactive domain, while any grid size larger than

0.5mm was shown to compromise the accuracy significantly [46]. The results of previous grid studies were shown to match the outcomes of a calibration study of the Sandia Flame D [54, 55], recommending Δs_{min} = 0.5mm as the acceptable grid resolution. In addition, comparison with *Converge CFD* commercial CFD code and detailed chemistry gave a similar outcome, defining Δs = 0.5mm as the acceptable grid threshold. Physical reason for that grid resolution requirement was provided in [54] to be the adequate resolution of turbulence-chemistry interaction in mixing controlled combustion processes.

3.2.2 Boundary Conditions

The centerline temperature from the main burner stage was determined in previous work [44, 45, 49, 56, 57] and verified to be a peak at 1800K for the present equivalence ratio φ = 0.75. This value is in good agreement with the temperature level determined for a 95% reaction progress level with the *Ansys Chemkin-Pro* model *1D Premixed Laminar Burner-Stabilized Flame* (T = 1820K). The measured temperature profile (Fig. 4) defines a second-order parabolic function between the centerline peak temperature T = 1800K and the inner wall temperature T = 500K. Velocity and turbulence intensity for the crossflow were measured with PIV data according to [50, 58]. The velocity profile in Fig. 4 follows a fourth-order parabolic function between a centerline velocity v = 58.5m/s and the wall v

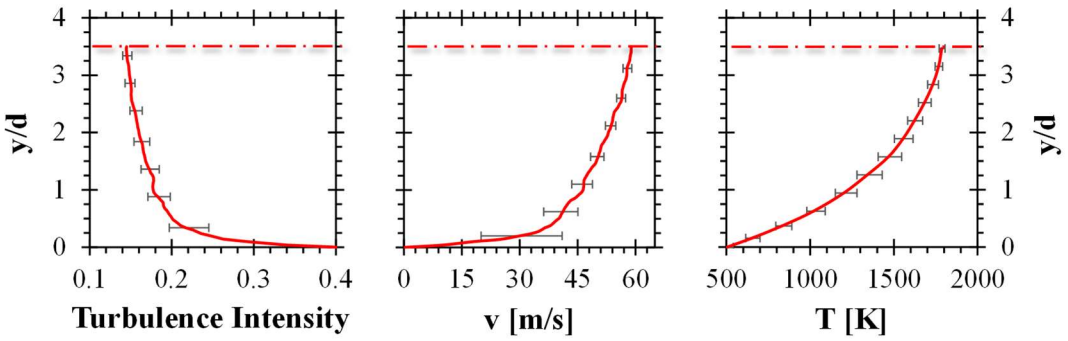

Figure 4: Experimental centerline boundary profiles for turbulence intensity, velocity, and temperature, characterizing the crossflow between combustion stages.

≈ 0. The turbulence intensity profile (fig. 4) defines a fourth-order parabolic function, with measured levels of 15% near the centerline, and up to 40% near the walls [50].

The jet boundary was defined as a premixed top-hat profile with turbulence intensity of 7% and mole fraction of diluent in the jet varied to substitute 0%, 15%, 30% and 50% of air, while holding the methane flow constant, as documented in Table 1. The axial jet was experimentally pre-heated and introduced to the test chamber at near-constant temperature level of 435K. In the CFD, the pre-heating section was not modeled, and the jet was assumed to be uniform in its temperature and composition profiles at the experimental flow straightener position. The crossflow boundary was defined at a validated 95% main burner equilibrium state. This reaction progress level was determined with temperature measurements at position A in Fig. 2, and species measurements taken for key species CO, CO_2 and O_2 at position A in Fig. 2. The oxides of nitrogen have longer kinetic formation timescales and were defined according to further emission measurements, taken at position (A). The measured main burner emissions at position (A) were 6ppmvd NO and 0.4ppmvd NO_2 (corrected to 15% O_2).

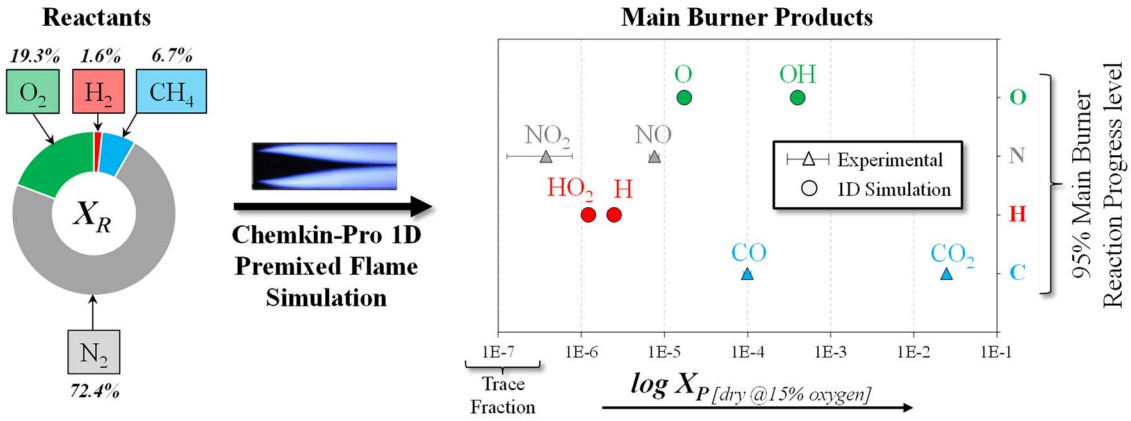

Figure 5: Main burner volumetric pollution species X_p to define the crossflow inlet boundary condition for 3D CFD. Product emission is measured (triangles) and the data complemented with Chemkin-Pro 1D premixed flame simulation (circles).

Additionally, the measured species composition was complemented with a few species that were not measured directly. These species at the investigated main burner condition p = 5atm, φ = 0.75 were determined by simulating a *1D Premixed Laminar Burner-Stabilized Flame* in *Ansys Chemkin-Pro* with 1D adaptive mesh refinement technique. According to the 1D model, the premixed near-equilibrium species composition contains O, OH, H and HO_2 in small quantities, yet above trace level, as shown in fig. 5. Therefore, fig, 5 shows the main burner fuel and air species composition, reacting in the premixed main burner stage to provide the hot, burnt crossflow boundary condition between the two burner stages. The data for the burnt composition was plotted on a log-scale on volumetric basis and provides the crossflow inlet boundary condition for the 3D CFD model, as shown in Fig. 2, position A. Note that all emission data stated in this paper is on dry basis and corrected to 15% oxygen level.

3.3 Test Conditions

A complete list of the test points presented in this paper is provided in Table 1. The conditions were simulated with detailed chemistry in *Star-CCM+* as well as characterized experimentally with the in-house setup, shown in Fig. 2. The operating points describe the collision of hot vitiated crossflow (T_{cf}^{max} = 1800K, v_{cf}^{max} = 58.5m/s) with a rich premixed axial jet. The diluent mass flow was either pure CO_2 or pure N_2, the volumetric percentage variation in the jet oxidizer was studied for 15%, 30% and 50% diluent. Jet densities range between 3.77 kg/m^3 for the baseline case, and up to 4.41 kg/m^3 with 50% axial CO_2 diluent addition. The momentum flux ratio depends on the jet density and was kept relatively constant at J = 8.5±0.5, providing a near-centered jet-in-crossflow for all test conditions.

Table 1: Experimental and Numerical Boundary Conditions

Vitiated Hot Crossflow between Burner Stages				
$\dot{m}_{cf}^{CH4}$ [g/s]	$\dot{m}_{cf}^{air}$ [g/s]	φ_{cf} [-]	*Centerline*	
			T_{cf} [K]	v_{cf} [m/s]
14.44	355.2	0.748	1800	58.5
Premixed Axial Jet Composition				
$\dot{m}_J^{CH4}$ [g/s]	$\dot{m}_J^{air}$ [g/s]	$\dot{m}_J^{diluent}$ [g/s]	T_J [K]	*% Diluent (CO_2 or N_2)*
3.35	33.0	n.a.	435	0%
	28.05	4.95		15%
	23.1	9.9		30%
	16.5	16.5		50%

The global average outlet temperature level 1700±5K was maintained for all conditions analyzed. The density ratio between the local minimum burnt density and the average crossflow density ranged between $\rho_{min}/\rho_{\infty} = 0.7$ for the baseline case, and $\rho_{min}/\rho_{\infty} = 0.8$ with 50% CO_2 diluent blending. A higher amount of added diluent resulted in a delayed axial combustion reaction with lower density gradients, lower local maximum temperature, and lower local and averaged nitric oxide emission.

4. RESULTS AND DISCUSSION

The results and discussion are presented in the following sections. In accordance with existing literature, the convention of jet penetration along the positive *y* axis shows the jet entering from the bottom in figs. 6 and 8.

4.1 Flame Lift-off Characteristics

Figure 6 shows a comparison between numerical and experimental flames, with respect to their lift-off characteristics. The experimental flame position is analyzed with CH* chemiluminescence data and compared with simulated CH levels in Fig. 6. Since the premixed thermal jet condition and penetration profile were kept relatively constant between diluent cases, the analysis in Fig. 6 is focused on the axial (x/d) flame lift-off. The iso-level at 20% of the maximal chemiluminescent intensity (I/I_{max} = 0.2) was extracted from the line-of-sight averaged CH* chemiluminescence data and compared with the 20% CFD iso-level of the simulated CH mole fraction. The ignition takes place near the z-symmetry plane, hence that plane was taken as a reference to process CH species from the averaged CFD cases. The experimentally measured CH* corresponds to the chemiluminescent emission from CH species at the similar position [50]. Hence, the measured CH* concentration follows the

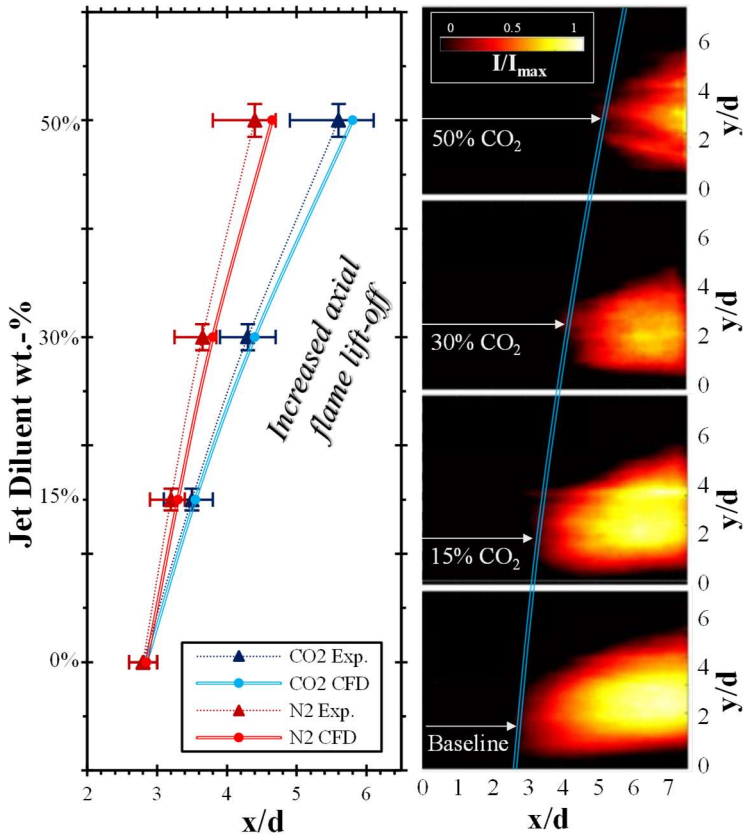

Figure 6: Axial flame lift-off as a function of axial jet diluent addition with jet entering from the bottom. a.) Simulated vs. experimental lift-off for N_2 and CO_2 diluents, b.) Experimental CH* flame contours with CO_2 diluent. Horizontal error bars: Range of measured axial lift-off, vertical error bars: flow meter uncertainty.

CH concentration in the flame, and a direct comparison with simulated CH species was deemed valid [59].

Figure 6 shows a good overlay between simulated and experimental data. The flame anchoring point for the baseline case was precisely captured by the detailed chemistry CFD, depicting the ignition point after 2.8 *x/d*. With increasing jet diluent, the ignition point is shifted further downstream. While the thermal conditions were kept relatively constant, the chemical driving force is reduced with higher diluent content due to the lower oxygen level in the jet. Increasing the diluent percentage led to a larger flame lift-off, which was coupled with a slight increase of modeled prediction uncertainty up to 8%. The CFD tends to ignite further downstream than the experiment, likely due to the challenge of fully resolving turbulence anisotropy further downstream from the jet. Unsteady turbulence-chemistry interactions for the high diluent cases along the Counter Rotating Vortex Pair (CVP) may not be fully captured, leading to a slightly late flame ignition in the model. The averaged axial ignition points at 20% of the maximal chemiluminescent intensity were captured after 4.4*d* (4.65*d* in the CFD) for 50% N_2 diluent and after 5.6*d* (5.8*d* in the CFD) for 50% CO_2 diluent. Addition of CO_2 diluent resulted in a higher axial lift-off, which could be influenced by the lower specific heat capacity of N_2 relative to CO_2. The deviations become more pronounced with high diluent content. N_2 cases were shown to ignite closer to the windward side of the jet, reducing the axial flame lift-off, whereas the averaged CO_2 imaging material showed a lee-side ignition further downstream (Fig. 6). Experimental uncertainty due to turbulent flame-flow fluctuation based on the unsteady CH* imaging series was determined to be ±0.2d for the baseline case, and up to ±0.6d for the 50% jet diluent cases (Fig. 6). The stabilization point of the experimental baseline case had low

fluctuation due to the early lee-side ignition and attached flame position. The increased fluctuations of the flame anchoring point for the highly diluted cases can be attributed to experimental observations of unsteady ignition dynamics for the leaner mixtures, while being exposed to enhanced three-dimensional effects along the evolving CVP.

4.2 Temperature and Emission Characteristics

Further analysis of the NO emission and correlation with the firing temperature profile is provided in the following sections. Table 2 states the simulated temperature and emission characteristics, and Fig. 7 provides an overlay between simulated and experimental CO and NO emission data. The local and averaged emission values are on a dry, volumetric basis (ppmvd) and corrected to 15% O_2. The O_2 correction used the *y,z*-averaged oxygen content at the respective axial position. The finite-rate detailed chemistry

Table 2: Temperature and emission characteristics as a function of diluent addition to the axial jet. Listed in parentheses and italics is the experimental validation data. Pollution levels are on dry, volumetric basis and corrected to 15% oxygen level.

Jet Diluent		**T_{max}** [K]	**NO_{max}** [ppmvd]	**$NO_{avg,out}$** [ppmvd]	**$CO_{avg,out}$** [ppmvd]
Baseline case		2100	55.6	15.9 *(16.0)*	20 *(19)*
15%	N_2	2071	49.9	15.0 *(14.8)*	29 *(28)*
30%	N_2	2023	42.5	13.3 *(13.4)*	38 *(36)*
50%	N_2	1965	36.1	12.0 *(12.2)*	53 *(50)*
15%	CO_2	2035	43.4	13.3 *(13.5)*	35 *(32)*
30%	CO_2	1975	32.6	11.4 *(11.5)*	51 *(48)*
50%	CO_2	1914	23.4	9.8 *(10.0)*	75 *(70)*

CFD coupled with the Eddy Dissipation Concept was found capable of describing NO emissions within 2% accuracy. Deviations between the measured and simulated CO emission levels amounted up to 7%.

As shown in Table 2 and Fig. 7, the measured, diluent-free baseline NO combustor emission level of 16.0ppmvd (15.9ppmvd simulated) could be reduced to 12.2ppmvd (12.0ppmvd simulated) with 50% N_2 jet diluent enrichment, and further reduced to 10.0ppmvd (9.8ppmvd simulated) with 50% CO_2 jet diluent enrichment. As described in section 3.2.1, the close overlay between simulated and measured data was achieved by using the Eddy Dissipation Concept, which reduces the reaction rate in finite-rate detailed chemistry problems, allowing to match the experimental lift-off and reaction progress levels (cf. Fig. 6). A nominally constant average firing temperature level of 1700±5K was maintained for all cases, since a constant amount of axial fuel was burned (cf. Table 1). However, local maximal temperatures in the axial stage depend strongly on the local reaction rates and were shown to decrease significantly with increasing axial diluent levels. A maximal simulated temperature of 2100K for the baseline case was reduced to 1965K with 50% N_2 jet diluent enrichment and reduced further to 1914K with 50% CO_2 jet diluent enrichment. These numbers justify the decrease in NO emissions with diluent addition, since thermal NO formation is a strong function of temperature, particularly at levels above T = 1700K.

The trade-off with decreased NO levels by diluent addition is the increasing CO emission, since CH_4 burnout would not be as complete as it could be at higher local temperature levels. CO emission increased from the diluent-free baseline case level

19ppmvd (20ppmvd simulated) to 50ppmvd (53ppmvd simulated) at 50% N_2 jet diluent

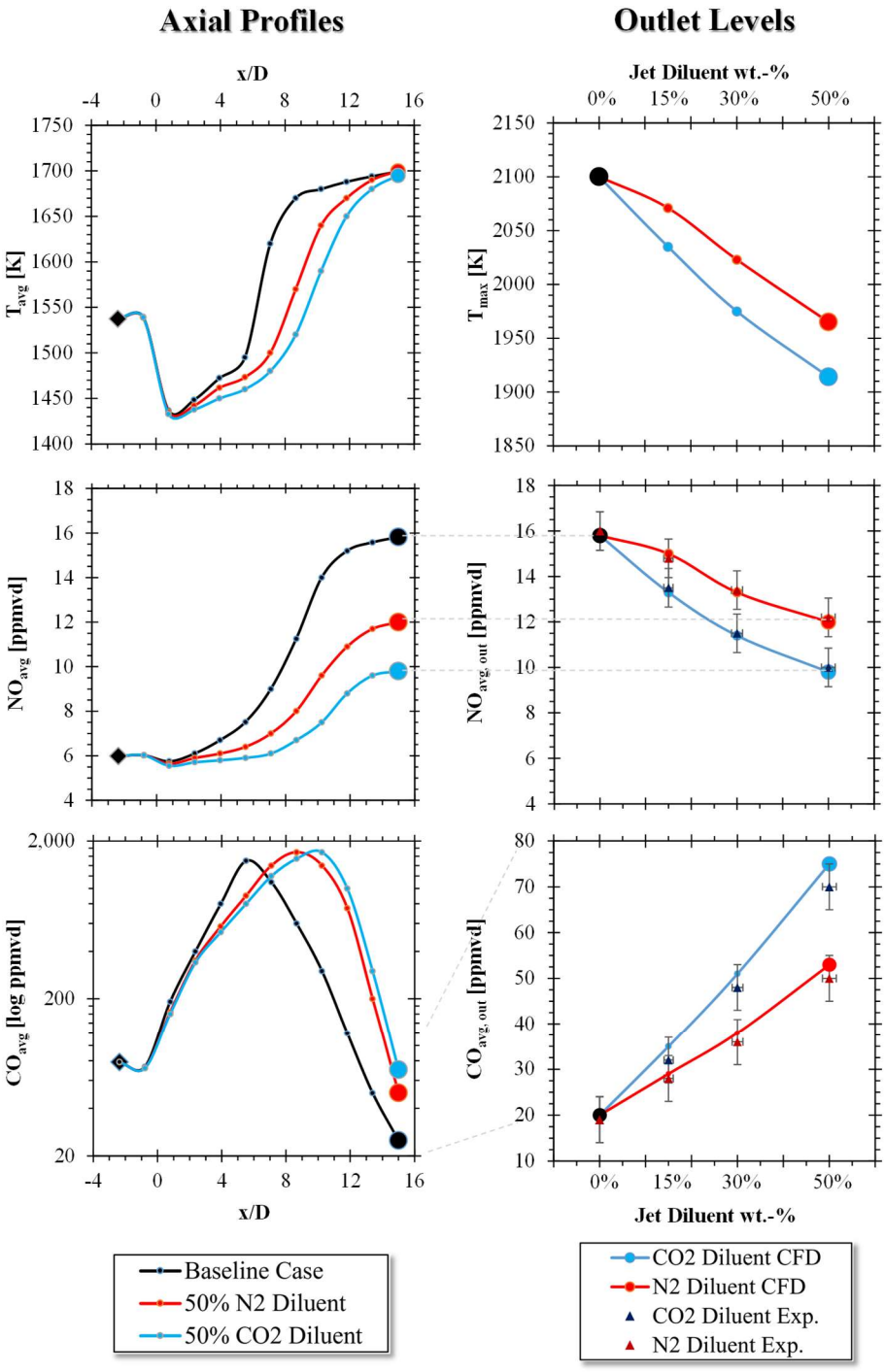

Figure 7: Left column: Extraction of simulated profiles along the y,z-averaged axial coordinate, with the jet entering at x/d = 0. Right column: Validation of simulated pollutant emission levels with experimental data taken at the combustor outlet (pos. B in fig. 2). Emission is on dry, volumetric basis and corrected to 15% oxygen level

enrichment, and to 70ppmvd (75ppmvd simulated) at 50% CO_2 jet diluent enrichment, respectively. This concerning trend outlines the need of careful tuning for commercial burner technology when using diluents, and possibly the utilization of an EGR strategy to reduce carbon oxide pollution by allowing more complete burnout prior to emission into the environment.

The left column of Fig. 7 shows the average temperature and emission levels along the axial coordinate downstream of the jet, comparing the baseline case (black line), 50% N_2 diluent case (red line), and 50% CO_2 diluent case (blue line). Temperature would initially decrease for all cases due to the introduction of relatively cold axial jet mixture at the position $x = 0$ (axial jet). Downstream of the jet, chemical reaction increases the average temperature to the average firing temperature level T = 1700±5 K for all cases. The reaction proceeds faster for the undiluted system, resulting in an earlier and steeper temperature rise profile relative to the diluted systems. The similar trends were picked up with the simulation for the average NO emission, with the outlet levels after 15 jet diameters highlighted with large round markers in Fig. 7. In contrast, the CO species profile along the axial coordinate was plotted on a log-scale due to the high intermediate CO levels along the $CH_4 \rightarrow CO \rightarrow CO_2$ reaction pathway. As shown by the CFD outcomes, tuning the combustor length is critical to achieve low CO emission levels.

Further analysis of the effect on the resulting firing temperature profiles and their correlation with NO emission profiles is provided in Fig 8. The baseline case (Fig. 8a.) and cases with 50% N_2 diluent (Fig. 8b.) and 50% CO_2 diluent level (Fig. 8c.) are shown at their positions of maximum temperature, located between 9 and 14 jet diameters downstream of the axial jet. For the baseline case, a maximum local temperature 2100K is

found near the windward shear layer along the counter rotating vortex pair after x/d = 9. The local temperature hotspot and strong windward emission formation are further amplified by the direct windward contact with the hot crossflow, producing up to 50ppmvd NO locally at this axial position. In contrast, the 50% N_2 diluent case burns at lower reaction progress rate (cf. Fig. 6), resulting in a lower maximum temperature 1965K after 12 axial jet diameters (Fig. 8b.). The profiles with 50% N_2 are more evenly distributed along the windward and lee-side shear layer. These results confirm the trends described in Fig. 7, coupling the more distributed temperature profile with lower NO emission levels [60], as occurring at high N_2 diluent content. The effect could be further pronounced with CO_2 diluent. Due to its larger heat capacity and further reduction of reaction rates, even more distributed temperature (T_{max} = 1914K) and NO emission profiles (23 ppmvd max.) were found at the *y,z*-contour position 14d. Concluding, the trend of increased jet diluent amount results in a more uniform firing temperature profile and correlates with lower NO and higher CO emission levels, as outlined in section 4.2. A more detailed analysis of simulated local reaction rate levels is provided in section 4.3 to gain insight to local emission formation kinetics.

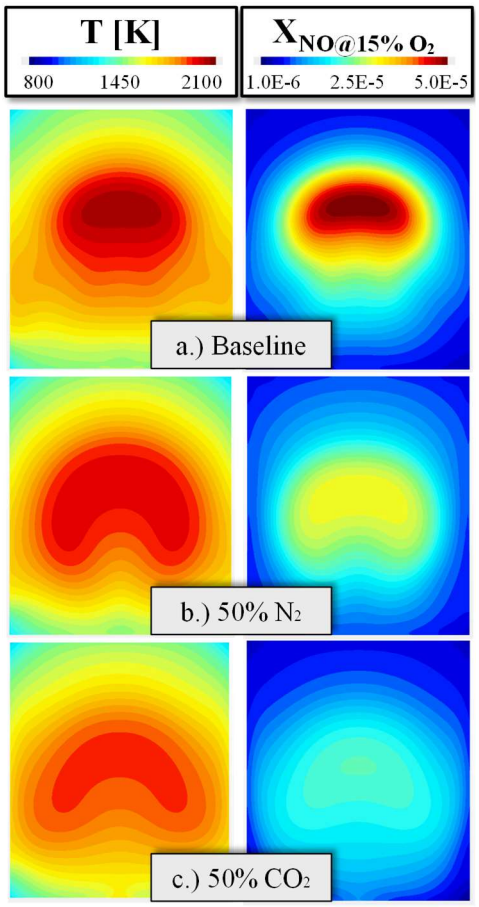

Figure 8: Correlation between firing temperature and nitric oxide (NO) emission profiles with jet entering from the bottom: a.) baseline case, b.) 50% N_2 jet diluent, c.) 50% CO_2 jet diluent

4.3 Maximum Pollutant Formation and Heat Release Rates

Having provided an overlay of experimental flame-flow characteristics, temperature and emission profiles, the following section is targeted to provide a numerical analysis of maximum volumetric windward and leeward heat release rate, as well as local reaction rates for key species involved in the production of nitric oxide emission in the axial combustor stage. The extracted CFD parameters in Fig. 9 include the maximum consumption rate of N_2 [$-r_{N2,\,max}$] in fig. 9a.), the maximum production rate of HCN [$r_{HCN,\,max}$] in fig. 9a.), as well as maxima for the windward and leeward NO production rates [$r_{NO,\,max}$] in fig. 9b.). The objective was to back out the amount of prompt NO produced relative to thermal NO. Additionally, fig. 9c.) shows the heat release rates [HRR_{max}] on a volumetric basis, as well as on volumetric basis normalized by pressure. The data is plotted at maximal rates, as occurring along the windward and leeward shear layers, in order to document the correlation between heat release rate and pollutant formation rate.

A critical objective was to determine the amount of near-flame NO, the so-called prompt NO emission, and quantify the impact of diluents on its local production rate. The prompt NO_x route is generally signified by the dissociation of molecular N_2, followed by the formation of the intermediates HCN, CN and NCN, and finally the formation of NO, NO_2, N_2O and other oxides of nitrogen. Since the formation rates of NO_2 and N_2O were at least a factor 50 below the NO production rates extracted, these were not focused on for the present study. Other prompt NO_x intermediates (CN etc.) were found to be 50 times smaller compared to the HCN route.

Figure 9a.) shows the overlay of maximal N_2 consumption rates and formation of HCN, proving the presence of the prompt NO route. Maximum HCN production rate of

0.032 kg/m^{3}s was found for the highly reactive baseline case. With diluent addition, these maximal rates were shown to decrease to a level 0.013 kg/m^{3}s with 50% N_2 diluent, and to 0.009 kg/m^{3}s with 50% CO_2 diluent, respectively. The curvature of maximal NO formation suggests an overlay of multiple effects, which remain governed strongly by local heat release (fig. 9c). By normalizing heat release with pressure, the heat release order of magnitude can be validated and compared with literature data at various pressure levels. Specifically, investigations by [61] stated the optimization of gas turbine relevant, diluted methane-air flames to potentially cover a range between 5E+6 W/m^{3}atm and 4.5E+8 W/m^{3}atm. The present study lies well within that range (fig. 9c), including conditions at peak heat rates between 1E+8 W/m^{3}atm and 3.5E+8 W/m^{3}atm.

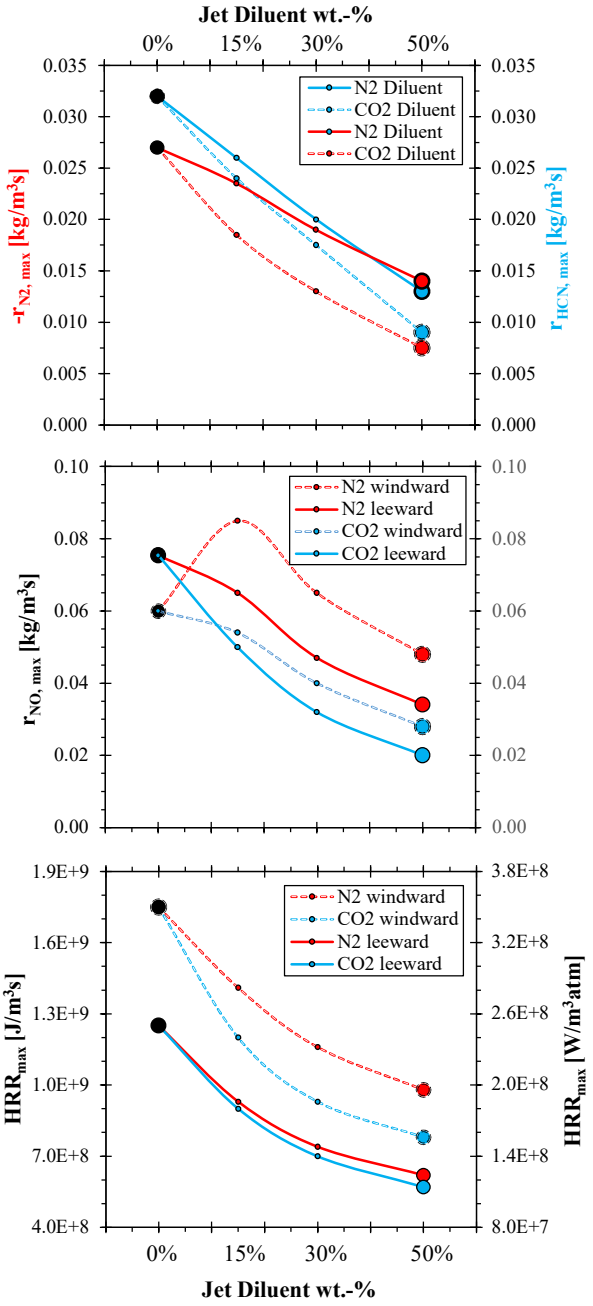

Figure 9: Maximum axial emission production rates and heat release as a function of added jet diluent

The significant reduction of maximal local production rates has indicated a prompt NO_x emission saving potential when diluents are used. Despite

the prompt NO_x benefit under diluent addition, two strong indicators to the dominance of thermal NO_x production were found in the analyzed system (Fig. 9):

1) HCN would only require a single N radical, but the dissociation of N_2 provides two N radicals at a time. Therefore, about 50% of N radicals shown in Fig. 9a.) would not be consumed towards the prompt NO route via HCN and are likely to form NO via the thermal mechanism.
2) Additionally, the maximal NO production rates (Fig. 9b.) outweighs the HCN production rates by a factor 2-3, at similar molecular masses of these species. Peak NO production rates are found along the windward shear layer, up to 0.085 kg/m^3s, whereas the maximal production of HCN was only 0.032 kg/m^3s.

Despite the challenges of backing out quantitative reaction pathways in turbulent combustion and NO_x pollutant formation, the present results suggest the combustion system to be thermal NO_x-dominated (est. 60-70%), even at the moderate average firing temperature level of T = 1700±5K. The results here emphasize on the overall NO emission reduction potential by blending diluent gas to the axial fuel jet and thus minimizing thermal NO_x, while estimating the contribution of prompt NO_x formation pathway to remain between 30 and 40%.

5. CONCLUSION

Rich premixed reacting jets in lean vitiated crossflow were investigated under variation of the diluent level, substituting 15%, 30% and 50% of the pre-heated axial air with pre-heated carbon dioxide or nitrogen diluent by mass percentage. Numerical investigation showed a near-constant momentum flux ratio J = 8.5±0.5 and global average

firing temperature level 1700±5K, allowing to isolate the diluent influence on the local temperature and associated nitric oxide emission profiles. The system responded to the increased diluent content with a delay in axial ignition, as well as a more uniform exit temperature profile. Nitric oxide (NO) emissions were reduced from a baseline-level 16.0ppmvd to 12.2ppmvd with 50% N_2 diluent, and reduced further to 10.0ppmvd with 50% CO_2 diluent. CO_2 can be considered a bulky inert component, acting as a thermal barrier along the reactive shear layer while hindering jet entrainment with hot oxidizer from the crossflow. Carbon monoxide (CO) emissions were increased with diluent addition from a baseline level 19ppmvd to 50ppmvd (50% N_2 diluent), and to 70ppmvd (50% CO_2 diluent). To increase the technology readiness level of such a system and maintain industrially tolerable CO emission levels of 25ppmvd or less, additional research could be performed to devise strategies to extract CO/CO_2 and N_2 from products and recirculate them into the combustor. Lastly, the impact of thermal NO_x and prompt NO_x formation routes was investigated under these high temperature firing conditions. The measured NO emission reduction potential with added jet diluent was tracked with maximal N-containing species reaction rate pathways. The major contribution of NO pollution was postulated to be thermal NO_x (60-70%), with subordinate contribution of the prompt NO_x pathway (30-40%).

Author Contributions

Bernhard Stiehl: Data curation, formal analysis, investigation, numerical methodology, writing – original draft. **Anthony Morales:** Investigation, experimental methodology, writing – reviewing and editing. **Tommy Genova Jr.:** Data curation,

investigation, experimental methodology, writing – reviewing and editing. **Michelle Otero:** Data curation, formal analysis, investigation. **Scott Martin:** Conceptualization, funding acquisition, Principal Investigator, supervision of experimental and numerical methodology, writing – reviewing and editing. **Changjin Yoon:** Industry Consultation, OEM Guidance. **Kareem Ahmed:** Conceptualization, Funding acquisition, supervision of experimental and numerical methodology.

Declaration of Competing Interest

The authors declare that they have no known competing financial interests or personal relationships that could have appeared to influence the work reported in this paper.

Acknowledgments

The authors (BS, AM, TG, MO, KA, SM and CY) acknowledge support from the *Department of Energy* under Award Number DE-FE0031227 and collaboration with *GE Global Research* under Dr. Dheeraj Kapilavai. The authors acknowledge *Siemens* and *Ansys* for product support and provision of academic licenses to their commercial simulation products *Star-CCM+* and *Chemkin-Pro*, respectively. The authors BS, AM and TG acknowledge research funding under the P3 Preeminent Postdoctoral Program, sponsored by the *University of Central Florida*.

information, apparatus, product, or process disclosed, or represents that its use would not infringe privately owned rights. Reference herein to any specific commercial product, process, or service by trade name, trademark, manufacturer, or otherwise does not necessarily constitute or imply its endorsement, recommendation, or favoring by the United States Government or any agency thereof. The views and opinions of authors expressed herein do not necessarily state or reflect those of the United States Government or any agency thereof.

REFERENCES

[1] Zeldovich, Y. B., Sadonikov, P. Y., Frank-Kamenetskii, D. A., 1947, "Oxidation of nitrogen in combustion (M. Shelef, Transl.)," Acad. Sci. USSR. Inst. Chem. Phys., Moscow–Leningrad.

[2] Zeldovich, Y. B., 1946, "The Oxidation of Nitrogen in Combustion Explosions," Acta Physicochimica U.S.S.R., 21, pp. 577–628.

[3] De Soete, G. G., 1975, "Overall reaction rates of NO and N2 formation from fuel nitrogen," 15th Symp. (Int'l.) on Combustion, 15(1), pp. 1093-1102.

[4] Blauvens, J., Smets, B., Peters, J., 1977, "The Combustion Institute," 16th Symp. (Int'l.) on Combustion.

[5] Fenimore, C. P., 1971, "Formation of Nitric Oxide in Premixed Hydrocarbon Flames," 13th Symp. (Int'l.) on Combustion, p. 373.

[6] Martin, S. M., Cai, W., Harris, J., 2013, "Apparatus and Method for Controlling the Secondary Injection of Fuel," Patent US 8,387,398 B2, Siemens Energy, Inc.

[7] Venkataraman, K. K., Terry, J. C., Velkur, C. B., Karim, H., 2014, "Late Lean Injection Fuel Staging Configurations," Patent US 8,707,707 B2, General Electric Company.

[8] Hutchins, A. R., Kribs, J. D., Lyons, K. M., 2015, "Effects of Diluents on Lifted Turbulent Methane and Ethylene Jet Flames," Journal of Energy Resources Technology, 137, p. 032204.

[9] Almansour, B., Thompson, L., Lopez, J., Barari, G., Vasu, S., 2016, "Laser Ignition and Flame Speed Measurements in Oxy-Methane Mixtures Diluted With CO2," Journal of Energy Resources Technology, 138, p. 032201.

[10] Desantes, J. M., Arrègle, J., López, J. J., and García, J. M., 2006, "Turbulent gas jets and diesel-like sprays in a crossflow: A study on axis deflection and air entrainment," Fuel, 85(14), pp. 2120-2132.

[11] Palacios, A., Bradley, D., and Hu, L., 2016, "Lift-off and blow-off of methane and propane subsonic vertical jet flames, with and without diluent air," Fuel, 183, pp. 414-419.

[12] Mordaunt, C. J., and Pierce, W. C., 2014, "Design and preliminary results of an atmospheric-pressure model gas turbine combustor utilizing varying CO2 doping concentration in CH4 to emulate biogas combustion," Fuel, 124, pp. 258-268.

[13] Lee, M. C., Seo, S. B., Yoon, J., Kim, M., and Yoon, Y., 2012, "Experimental study on the effect of N2, CO2, and steam dilution on the combustion performance of H2 and CO synthetic gas in an industrial gas turbine," Fuel, 102, pp. 431-438.

[14] Jourdaine, P., Mirat, C., Caudal, J., Lo, A., and Schuller, T., 2017, "A comparison between the stabilization of premixed swirling CO2-diluted methane oxy-flames and methane/air flames," Fuel, 201, pp. 156-164.

[15] Duan, X., Li, Y., Liu, Y., Zhang, S., Guan, J., Lai, M.-C., and Liu, J., 2020, "Dilution gas and hydrogen enrichment on the laminar flame speed and flame structure of the methane/air mixture," Fuel, 281, p. 118794.

[16] Khan, A. R., Anbusaravanan, S., Kalathi, L., Velamati, R., and Prathap, C., 2017, "Investigation of dilution effect with N2/CO2 on laminar burning velocity of premixed methane/oxygen mixtures using freely expanding spherical flames," Fuel, 196, pp. 225-232.

[17] Wang, S., Wang, Z., Han, X., Chen, C., He, Y., Zhu, Y., and Cen, K., 2020, "Experimental and numerical study of the effect of elevated pressure on laminar burning velocity of lean H2/CO/O2/diluents flames," Fuel, 273, p. 117753.

[18] Huang, W., 2015, "Effect of jet-to-crossflow pressure ratio arrangement on turbulent mixing in a flowpath with square staged injectors," Fuel, 144, pp. 164-170.

[19] Duva, B. C., Chance, L. E., and Toulson, E., 2020, "Dilution effect of different combustion residuals on laminar burning velocities and burned gas Markstein lengths of premixed methane/air mixtures at elevated temperature," Fuel, 267, p. 117153.

[20] Duva, B. C., Wang, Y. C., Chance, L. E., and Toulson, E., 2020, "Correlations for the laminar burning velocity and burned gas Markstein length of methane-air mixtures diluted with flue gases at high temperatures and pressures," Fuel, 281, p. 118721.

[21] Smith, G. P., Golden, D. M., Frenklach, M., Moriarty, N. W., Eiteneer, B., Goldenberg, M., Bowman, C. T., Hanson, R. K., Song, S., Gardiner, Jr., W. C. Lissianski, V. V. and Qin, Z., "GRI-MECH 3.0," http://www.me.berkeley.edu/gri_mech/.

[22] Metcalfe, W. K., Burke, S. M., Ahmed, S. S., Curran, H. J., 2013, "A Hierarchical and Comparative Kinetic Modeling Study of C1 − C2 Hydrocarbon and Oxygenated Fuels," International Journal of Chemical Kinetics, 45(10), pp. 638–675.

[23] El Merhubi, H., Kéromnès, A., Catalano, G., Lefort, B., and Le Moyne, L., 2016, "A high pressure experimental and numerical study of methane ignition," Fuel, 177, pp. 164-172.

[24] Yossefi, D., Ashcroft, S. J., Hacohen, J., Belmont, M. R., and Thorpe, I., 1995, "Combustion of methane and ethane with CO2 replacing N2 as a diluent. Modelling of combined effects of detailed chemical kinetics and thermal properties on the early stages of combustion," Fuel, 74(7), pp. 1061-1071.

[25] Su, J., Wu, Y., Wang, Y., Chen, X., and Chen, Z., 2021, "Skeletal and reduced kinetic models for methane oxidation under engine-relevant conditions," Fuel, 288, p. 119667.

[26] Shu, Z., Dai, C., Li, P., and Mi, J., 2018, "Nitric oxide of MILD combustion of a methane jet flame in hot oxidizer coflow: Its formations and emissions under H2O, CO2 and N2 dilutions," Fuel, 234, pp. 567-580.

[27] Huang, M., Li, R., Xu, J., Cheng, S., Deng, H., Rong, Z., Li, Y., and Zhang, Y., 2022, "Effect of equivalence ratio and staging ratio on the methane MILD combustion in dual-stage combustor," Fuel, 307, p. 121903.

[28] Kim, T. H., Park, J. W., Park, H. Y., Park, J., Park, J. H., and Lim, I. G., 2016, "Chemical and radiation effects on flame extinction and NOx formation in oxy-methane combustion diluted with CO2," Fuel, 177, pp. 235-243.

[29] Khalil, A. E. E., and Gupta, A. K., 2016, "Fuel property effects on distributed combustion," Fuel, 171, pp. 116-124.

[30] Spliethoff, H., Greul, U., Rüdiger, H., and Hein, K. R. G., 1996, "Basic effects on NOx emissions in air staging and reburning at a bench-scale test facility," Fuel, 75(5), pp. 560-564.

[31] Khalil, A. E. E., and Gupta, A. K., 2016, "On the flame–flow interaction under distributed combustion conditions," Fuel, 182, pp. 17-26.

[32] Khalil, A. E. E., and Gupta, A. K., 2015, "Toward ultra-low emission distributed combustion with fuel air dilution," Applied Energy, 148, pp. 187-195.

[33] Feser, J. S., Karyeyen, S., and Gupta, A. K., 2020, "Flowfield impact on distributed combustion in a swirl assisted burner," Fuel, 263, p. 116643.

[34] Khalil, A. E. E., and Gupta, A. K., 2018, "Fostering distributed combustion in a swirl burner using prevaporized liquid fuels," Applied Energy, 211, pp. 513-522.

[35] Khalil, A. E. E., and Gupta, A. K., 2017, "Flame fluctuations in Oxy-CO2-methane mixtures in swirl assisted distributed combustion," Applied Energy, 204, pp. 303-317.

[36] Karyeyen, S., Feser, J. S., and Gupta, A. K., 2019, "Hydrogen concentration effects on swirl-stabilized oxy-colorless distributed combustion," Fuel, 253, pp. 772-780.

[37] Khalil, A. E. E., and Gupta, A. K., 2017, "The role of CO2 on oxy-colorless distributed combustion," Applied Energy, 188, pp. 466-474.

[38] Khalil, A. E. E., and Gupta, A. K., 2017, "Towards colorless distributed combustion regime," Fuel, 195, pp. 113-122.

[39] Khalil, A. E. E., and Gupta, A. K., 2015, "Internal entrainment effects on high intensity distributed combustion using non-intrusive diagnostics," Applied Energy, 160, pp. 467-476.

[40] Roy, R., and Gupta, A. K., 2020, "Flame structure and emission signature in distributed combustion," Fuel, 262, p. 116460.

[41] Zhang, L., Ren, X., Sun, R., Levendis, Y. A., 2020, "A Numerical and Experimental Study on the Effects of CO2 on Laminar Diffusion Methane/AirFlames," Journal of Energy Resources Technology, 142, p. 082307.

[42] Stiehl, B., Genova, T., Otero, M., Reyes, J., Ahmed, K.A., Martin, S.M., 2020, "NOx Emission of an Axial-Staged Combustor at High-Pressure," AIAA Propulsion and Energy 2020 Forum.

[43] Otero, M., Stiehl, B., Genova, T., Ahmed, K., Martin, S., 2020, "Premixed Reacting Jet Flow Behavior in an Axially Staged Model Combustor at Elevated Pressure," AIAA Propulsion and Energy 2020 Forum.

[44] Otero, M., Genova, T., Ahmed, K., Stiehl, B., Vasu, S., Martin, S., 2019, "Characteristics of a Premixed Reacting Jet-in-Crossflow at Elevated Pressures," AIAA Propulsion and Energy 2019 Forum.

[45] Otero, M., Genova, T., Reyes, J., Stiehl, B., Ahmed, K., Martin, S., 2019, "Characteristics of a Reacting Jet-in-Crossflow at Elevated Pressures," AIAA Propulsion and Energy 2019 Forum.

[46] Stiehl, B., Otero, M., Genova, T., Martin, S., Ahmed, K., 2021, "Fuel Stratification Influence on NOx Emission in a Premixed Axial Reacting Jet-in-Crossflow at High Pressure," Journal of Energy Resources Technology.

[47] Otero, M., Genova, T., Stiehl, B., Morales, A., Martin, S., Ahmed, K., 2022, "The Influence of Pressure on Flame-Flow Characteristics of a Reacting Jet in Crossflow," Journal of Energy Resources Technology.

[48] Genova, T., Otero, M., Morales, A., Stiehl, B., Martin, S., and Ahmed, K., 2021, "Preheating and premixing effects on NOx emissions in a high-pressure axially staged combustor," Combustion and Flame, p. 111710.

[49] Genova, T., Stiehl, B., Otero, M., Ahmed, K., Martin, S., 2020, "Experimental and Numerical Investigation of a High-Pressure Reacting Jet-in-Crossflow," AIAA Propulsion and Energy 2020 Forum.

[50] Stiehl, B., Otero, M., Genova, T., Martin, S., Ahmed, K., 2021, "The Effect of Pressure on NOx Entitlement and Reaction Timescales in a Premixed Axial Jet-in-Crossflow," Journal of Energy Resources Technology.

[51] Stiehl, B., Worbington, T., Miegel, A., Martin, S., Velez, C., Ahmed, K., 2019, "Combustion and Emission Characteristics of a Lean Axial-Stage Combustor," Proceedings of ASME TurboExpo 2019.

[52] Prathap, C., Galeazzo, F. C. C., Kasabov, P., Habisreuther, P., Zarzalis, N., Beck, C., Krebs, W., Wegner, B., 2012, "Analysis of NOx Formation in an Axially Staged Combustion System at Elevated Pressure Conditions," J. Eng. Gas Turbines Power, 134(3).

[53] Stiehl, B., Worbington, T., Woodard, A., Ahmed, K., 2020, "Numerical Simulation of an Axial-Staged Combustor at High Pressure," 2020 AIAA SciTech Forum and Exposition.

[54] Software, C. C., 2018, "Resolving Turbulence-Chemistry Interactions in Mixing-Controlled Combustion with LES and Detailed Chemistry."

[55] Stiehl, B., 2020, "Numerical Investigation of Reacting Jet-in-Crossflow at High Pressure," University of Central Florida Dissertation.

[56] Genova, T., Otero, M., Stiehl, B., Reyes, J., Ahmed, K., Martin, S., 2019, "Exploration of a Reacting Jet-in-Crossflow in a High-Pressure Axial Stage Combustor," AIAA Propulsion and Energy 2019 Forum.

[57] Genova, T., Otero, M., Reyes, J., Martin, S., Ahmed, K. A., 2021, "Partial Premixing Effects on the Reacting Jet of a High Pressure Axially Staged Combustor," Journal of Engineering for Gas Turbines and Power.

[58] Otero, M., Genova, T., Stiehl, B., Morales, A., Martin, S., and Ahmed, K., 2022, "The Influence of Pressure on Flame-Flow Characteristics of a Reacting Jet in Crossflow," Journal of Energy Resources Technology, pp. 1-30.

[59] Nori, V. N., Seitzman, J. M., 2009, "CH* chemiluminescence modeling for combustion diagnostics," Proceedings of the Combustion Institute, 32, pp. 895–903.

[60] EPA, 1999, "Nitrogen Oxides (NOx), Why and How They Are Controlled," United States Environmental Protection Agency EPA-456/F-99-006R.

[61] Arghode, V. K., and Gupta, A. K., 2013, "Role of thermal intensity on operational characteristics of ultra-low emission colorless distributed combustion," Applied Energy, 111, pp. 930-956.